RSC Advances

ROYAL SOCIETY OF CHEMISTRY

www.rsc.org/advances

A novel photocatalyst CeF_3: Facile fabrication and photocatalytic performance

Hui Miao, Gui-Fang Huang*, Liang Xu, Yin-Cai Yang, Ke Yang, Wei-Qing Huang#

Department of Applied Physics, School of Physics and Electronics, Hunan University, Changsha 410082, China

Abstract: The pursuit of semiconductor photocatalysts with outstanding performance has stimulated increasing efforts to explore novel materials to address problems in environmental remediation and energy utilization. Herein, we first report the synthesis of CeF_3 nanoparticles by a facile low-temperature solution combustion method and its performance for photocatalytic degradation of methylene blue (MB) under UV light irradiation. Interestingly, only by adjusting the molar ratios of ammonium fluoride to cerium chloride, pure CeF_3 nanoparticles, its mixture with CeO_2 and/or Ce_2O_3, and pure CeO_2 nanoparticles can be easily obtained, respectively. The synthesized CeF_3 nanoparticles can effectively decompose organic contaminants in aqueous solution and show enhanced photocatalytic activity than CeO_2 nanoparticles. Moreover, CeF_3 exhibits high stability. The density functional theory (DFT) calculation has been performed to understand the photocatalysis mechanism of CeF_3 nanoparticles. This research might provide some new insights for the synthesis of novel photocatalyst with high photocatalytic performance.

Keywords: CeF_3, photocatalytic activity, solution combustion method, novel photocatalyst

1. Introduction

Photocatalytic semiconductors have attracted increasing attention due to their potential applications in renewable energy production and environmental purification by utilizing solar energy[1-4]. Among the various photocatalysts, TiO_2, the undoubtedly typical and most promising photocatalyst, has been the focus in this field owing to its biological and chemical inertness, cost

*.Corresponding author. *E-mail address:* gfhuang@hnu.edu.cn
#.Corresponding author. *E-mail address:* wqhuang@hnu.edu.cn

effectiveness, nontoxicity, and high stability[5]. However, its large band gap and the rapid recombination of photogenerated electrons and holes result in the inefficient use of solar energy and low energy efficiency. Therefore, many studies have been performed to modify TiO_2[6-9] or to seek new efficient photocatalytic materials[2, 9, 10].

So far, more than 190 different semiconductor materials have been reported to show activity for the photodegradation of organic pollutants or/and water splitting[11-14]. As well-known functional rare-earth metal compounds, cerium-containing nanomaterials have attracted great interest owing to their technological applications and fundamental scientific importance. Among the cerium-containing compounds, CeO_2 and CeF_3 are two of the typical materials with wide applications in solid-state fuel cells[15], catalysts[9, 16-18], polishing materials[4], and so on. It is found that the CeO_2 hierarchical nanorods and nanowires synthesized by electrochemical method exhibit substantially higher photocatalytic performance than the commercial CeO_2 nanoparticles in the degradation of methyl orange[9]. Mao and his coworks find that the N-doped CeO_2 nanoparticles possess much higher visible-light sensitivity and enhanced photocatalytic activity compared to pure CeO_2[19]. Moreover, the activity of CeO_2 for the photocatalytic degradation of azodye acid orange 7[20] and MB[21] is much higher than that of the commercial TiO_2 P25, indicating that CeO_2 can be used as an effective photocatalyst for environmental remediation.

CeF_3 is regarded as an important inorganic material in various fields, such as photocatalytic technology[22], sensors[23], optical components[24] and solid lubricants[25], due to its fast response, high ionic conductivity and unique optical property. In comparison with oxygen-based systems, fluorides possess very low vibrational energies, therefore, the quenching of the excited states of the rare earth ions may be minimal and CeF_3 is usually considered as luminescent material[26,27]. The recent experiment has demonstrated that the CeF_3/TiO_2 is a more effective photocatalyst for CO_2 reduction under visible light than pure TiO_2[22]. However, the study on the photocatalytic activity of pure CeF_3 as a potential photocatalyst has never been reported before. Therefore, it is of great interest to investigate the photocatalytic properties of CeF_3 material.

In this work, CeF_3 and CeO_2 nanoparticles are synthesized by a facile low-temperature solution combustion method. It is interesting that pure CeO_2, CeF_3 and their mixture can be easily obtained by adjusting the molar ratio of ammonium fluoride to cerium chloride. The

photocatalytic activity of the prepared samples is evaluated by degrading MB under UV light irradiation. The results demonstrate that CeF_3 shows enhanced photocatalytic activity and can be used as potential photocatalyst.

2. Experimental section

2.1 Preparation of samples

CeF_3 and CeO_2 nanoparticles are synthesized by low-temperature solution combustion method using citric acid as fuel. All the chemicals are of analytical grade and used as received without further purification. In a typical synthesis process, appropriate ammonium fluoride is dispersed into 20 mL deionized water, followed by addition of 1.86 g cerium chloride heptahydrate, 1.6 g citric acid monohydrate and 2 mL concentrated nitric acid into the every solution under constant stirring at room temperature. The resultant homogeneous solution is transferred into a crucible. Then, the crucible is put into a muffle furnace and heated at 300 ℃ for about half an hour. Finally, the synthesized samples are washed with distilled water and alcohol, and annealed at 500 ℃ in air for 2h. Samples with different molar ratios of ammonium fluoride to cerium chloride (0, 1, 5, 10, 12.5 and 20) are synthesized to investigate the effect of compositions on the structure and photocatalytic performances. The samples with molar ratio of 0, 5, 10 and 20 are marked as samples A, B, C and D, respectively.

2.2 Characterizations

The X-ray diffraction patterns (XRD) of samples are measured using Siemens D-5000 diffractometer with Cu Kα irradiation. The morphological details of the prepared samples are probed by an S-4800 field emission scanning electron microscopy (FESEM). The composition of sample B is analyzed by the energy dispersive spectroscopy (EDS) attached to SEM. The Brunauer-Emmett-Teller (BET) specific surface area of the products is analyzed by nitrogen adsorption in a Micromeritics ASAP 2020 nitrogen adsorption apparatus. The optical absorption spectra of the samples are recorded using a UV/VIS spectrometer (UV-2450, Shimadzu).

2.3 Photocatalytic degradation of MB

The photocatalytic activities of prepared samples are evaluated by the degradation of MB (10

mg/L, 80 mL) with 30 mg of the photocatalysts under irradiation of 300 W UV lamp. Before irradiation, solutions suspended with photocatalysts are sonicated in the dark for 20 minutes to ensure the adsorption-desorption equilibrium of MB on the surface of photocatalysts. During the irradiation, 5 mL suspension is withdrawn at regular time intervals and centrifuged to remove the photocatalysts. The photodegradation efficiency is monitored by measuring the absorbance of the solution samples at its characteristic absorption wavelength with a UV-Vis spectrophotometer at room temperature. The degradation efficiency can be evaluated by the function $C_t/C_0 \times 100\%$, where C_0 is the initial concentration of MB and C_t is the concentration after degradation. For comparison, the self-degradation of MB in dark or under UV light irradiation and the photocatalytic activity of commercial P25 is also explored in the same condition.

In order to examine the stability of CeF_3, the recycling experiments are carried out under the identical conditions. Each degradation cycle lasts for 30min, after each photodegradation cycle, the CeF_3 photocatalyst is collected by centrifugation, washed with distilled water and alcohol several times, and reused in the following run to repeat the same degradation experiment.

2.4. Computational details

All of the density-functional theory (DFT) calculations have been performed using the frozen-core projector-augmented-wave (PAW) method within the local density approximation (LDA). The quantitative prediction for the chemical and physical properties of CeO_2 and CeF_3 requires an accurate description of its 4f states. A simple, empirical and weakly-demanding computational approach to obtain appropriate band structure is to add an on-site coulombic repulsion term, leading to the so-called DFT+U approach, which has shown a wide use in studying bulk CeO_2 and its composite. For CeO_2, the calculated structural parameters, band gap, and the levels in the vicinity to Fermi level obtained from LDA+U, PBE0, and HSE06 are in agreement with each other and coincided with experimental results. Therefore, we choose the DFT/LDA+U method. The extensive tests have been performed to determine the appropriate Hubbard U parameters (Ce 4f and O 2p are 9.0 and 4.5 eV, respectively), which reproduced the correct lattice parameters (5.40 Å) and energy gap (3.2 eV) for cubic CeO_2. Considering the similarity of F and O elements, the U value of F 2p is also taken as 4.5 eV. The valence atomic configurations are Ce: $4f^1\ 5d^1\ 6s^2$, O: $2s^2\ 2p^4$, and F: $2S^2\ 2p^5$, respectively. The models are relaxed without any symmetry

constraints with a cutoff energy of 500 eV. The convergence of energy and force are set to 10^{-6} eV and 0.01eV/Å, respectively.

3. Results and discussion

3.1 Morphology and structure characterization

Generally, the morphology and size of nanoparticles have a great impact on their performance. The morphologies and chemical composition of samples are detected by SEM and EDS, respectively. The typical SEM images of prepared samples A, B, C and D are depicted in Fig.1. It can be seen from Fig. 1 (a) that sample A is composed of irregular particles with size of about 60-120 nm. While there are vast nanoparticles interspersed with some large particles for sample B as shown in Fig. 1 (b), suggesting the existence of two phases in sample B. With further increasing the molar ratios of ammonium fluoride to cerium chloride, it can be clearly observed that samples C (Fig. 1 (c)) and D (Fig. 1 (d)) are composed of nanoparticles which agglomerate to some extent.

The EDS spectrum of sample B illustrated in Fig. 2 clearly shows that there are only Ce, O and F elements are detected. The atomic ratio of Ce, O and F is 24.29, 11.12 and 64.58%, respectively, suggesting that rare-earth metal cerium remains in fluoride and oxides.

XRD is employed to investigate the structural information of the prepared samples. The XRD patterns of samples synthesized with different ratio of ammonium fluoride are displayed in Fig.3. The presence of well defined peaks, as illustrated in Fig. 3, reveals the polycrystalline nature of prepared samples. All the diffraction peaks of the sample synthesized without the addition of ammonium fluoride can be assigned to the diffractions of the (111), (200), (220), (311), (222), (400), (331) and (420) planes of the cubic CeO_2(JCPDS Card no. 34-0394). No other peaks can be observed, suggesting the formation of pure CeO_2 in sample A. As the molar ratio of ammonium fluoride to cerium chloride increases to 5, the XRD pattern of the sample B includes the patterns of CeO_2 (JCPDS Card no. 34-0394) and CeF_3 (JCPDS Card no. 08-0045). In addition, the weak peaks observed at 26.62^o and 75.12^o in samples B and C can be assigned to the (100) and (203) planes of Ce_2O_3 (JCPDS Card no.23-1084). This is match with the SEM images and EDS measurement. With further increase the molar ratio of ammonium fluoride to cerium chloride, one

can notice that all the diffraction peaks can be attributed to CeF_3 in hexagonal phase, indicating that pure CeF_3 is obtained.

Fig. 4 (a) gives the UV-visible absorption spectra of pure CeO_2 (sample A) and pure CeF_3 (sample C). It can be seen that the CeO_2 nanoparticles exhibit a steep increase in absorption at wavelength of about 400 nm. Whereas CeF_3 nanoparticles display a slow increase in absorption in the visible light and ultraviolet ranges, implying that the prepared CeF_3 nanoparticles are responsive in the whole wavelength range. The appearance of visible light absorbance of CeF_3 in UV-visible absorption spectrum might be attributed to the defects and the distorted lattices[27]. Normally, CeF_3 is studied as luminescent material. It is reported that the defects existed in CeF_3 nanoparticles are responsible for the decrease in the luminescence intensity[27, 28]. As is well known, the defects existed in semiconductors play a significant role in the light absorption and the corresponding photocatalytic performance[29, 30]. Thus, the visible light absorbance of CeF_3 in UV-visible absorption spectrum might be closely related to its defects. The effects of the defects and the distorted lattices on the visible light absorption will be further discussed in detail in Section 3.3.

It is considered that the energy level and band gap of the semiconductors play a crucial role in determining its photocatalytic activity. Thus the band gap (Eg) of the prepared CeO_2 and CeF_3 is calculated using the following relationship:

$$\alpha h\nu = A(h\nu - E_g)^2$$

Where a, h, ν, Eg and A are absorption coefficient, Planck constant, light frequency, band gap energy, and a constant, respectively.

One can infer the material band gap from the intercept of the extrapolated linear region of plots of $(\alpha h\nu)^2$ versus energy $h\nu$ on the energy axis, as shown in Fig.4 (b), the roughly estimated indirect band gaps of CeO_2 is about 3.23 eV, which are similar to the previous literature[2]. The band gap of CeF_3 is calculated to be about 3.32 eV, which is slightly larger than that of CeO_2.

3.2 Photocatalytic activity for the degradation of MB

As is known, the prerequisite for efficient photodegradation pathway is the pre-adsorption of organic dye molecules on the photocatalyst surface. The BET surface areas of the photocatalysts

are determined by the nitrogen adsorption experiments. Fig. 5 shows the nitrogen adsorption–desorption isotherms of sample C. Typically, CeF_3 shows isotherms of type IV with a hysteresis loop according to the Brunauer-Deming-Deming-Teller classification. The isotherm exhibits a linear absorption in the low relative pressure range ($P/P_0<0.7$), and an obvious hysteresis in the high relative pressure range ($0.7<P/P_0<1$), indicating the presence of mesopores. The plot of the pore-diameter distribution is determined from the desorption branch of the isotherm using the Barrett–Joyner–Halenda (BJH) method. The BJH pore diameter distribution in the inset of Fig. 5 indicates the existence of mesopores with peak at approximately 4 nm. The value of the BET surface area is up to 11.3 m^2 g^{-1} for CeF_3, which is similar to that of CeF_3 nanoparticles prepared by sonication assisted method[31].

To elucidate the photocatalytic performances of the prepared samples, photocatalytic degradation of MB is chosen as the probe reaction since MB is usually selected as a typical organic pollutant to test the activity of photocatalysts. The samples are mixed with the MB solution and sonicated in the dark for 20 minutes to reach the adsorption-desorption equilibrium of MB on the surface of photocatalysts. Time dependence of the UV–Vis spectra in photodegradation of MB over sample C is illustrated in Fig. 6 (a). It is clear that the characteristic absorbance peak decreases after 20 minutes' ultrasonic treatment and further decreases with the increased irradiation time, suggesting that part of MB molecules are adsorbed on the surface when the adsorption-desorption equilibrium reach. The further decrease of the characteristic absorbance peak of MB with irradiation time indicates the photodegradation of MB.

The photocatalytic performance of the prepared samples and commercial P25 is evaluated and the change of the MB concentration during the photo-degradation process is shown in Fig. 6(b). As a comparison, MB degradation with no catalyst is also carried out in dark or under the identical conditions. It is found that the degradation efficiency of MB without photocatalyst is negligible in dark, testifying the stabilization of MB. The degradation efficiency of MB under UV light irradiation increases with the irradiation time, however, the degradation efficiency of MB without a photocatalyst is relatively slow. After 30 min UV light irradiation, only about 18% of MB is photodegraded in the absence of photocatalyst as shown in Fig. 6(b). The slow self-degradation of MB under UV light is similar to the previous report[32]. In contrast, the presence

of photocatalyst will greatly accelerate the degradation of MB. It can be observed that about 55% of the initial dyes are degraded after 30 min UV light irradiation for CeO_2 (sample A). Moreover, the photocatalytic activity is enhanced with the molar ratio increase, and CeF_3 (sample C) shows much enhanced photocatalytic activity in the photodegradation of MB, 90% of the initial dyes are degraded after 30 min UV light irradiation. As can be seen from Fig. 6(b), the photocatalytic activity of the prepared CeF_3 is close to that of commercial P25. Therefore, CeF_3 as a novel photocatalyst shows great application potential in photocatalysis.

The kinetic curves for MB photocatalytic degradation with different photocatalysts are plotted and presented in Fig. 6(c). It can be observed that the relationship between $\ln(C_0/C_t)$ and irradiation time is almost linear, suggesting the photocatalytic reaction follows the pseudo-fist-order kinetics. According to Langmuir-Hinshelwood model, the apparent reaction rate constant k of MB decomposition under UV light irradiation without photocatalyst is about 0.00687 min^{-1}. While the apparent reaction rate constants k of MB decomposition over samples increase obviously, and the value of k over samples with molar ratios of ammonium fluoride to cerium chloride of 0, 1, 5, 10, 12.5 to 20 are estimated to be about 0.0334 min^{-1}, 0.04398 min^{-1}, 0.06301 min^{-1}, 0.0874 min^{-1}, 0.07812 min^{-1} and 0.04927 min^{-1}, respectively. From the photodegradation constant k, one can easily compare the photocatalytic performance of different samples. The degradation efficiency of CeF_3 (samples C) is more than twice that of CeO_2 (samples A).

It is well known that stability of the photocatalyst is crucially important for the practical applications. To evaluate the stability of CeF_3, the recycle experiment under identical conditions is carried out. As shown in Fig. 7, the degradation rate of MB is up to 88% over CeF_3 photocatalyst under UV light irradiation after the third run, which is similar to that in the first run. The results show that CeF_3 photocatalyst exhibit good stability for the UV light degradation of MB.

3.3 Density of states and photocatalysis mechanism

It is known that the fundamental process of semiconductor photocatalysis involves the formation of electron-hole pairs under light irradiation, and the subsequent migration of the photoinduced carriers to the surfaces of semiconductor, which will produce the redox sources of

• O_2^- and •OH radical species by reacting with the adsorbed O_2 and H_2O and lead to the destruction of organic pollutants. Thus, the photocatalytic activity of photocatalysts is highly dependent on their band structures and charge transfer dynamics.

In order to further clarify the photocatalytic mechanism of CeF_3, the electronic structure of CeF_3 is explored by employing DFT. Fig. 8 plots the density of state (DOS) and the projected DOS (PDOS) of CeF_3 and CeO_2, and the band structure of CeF_3. The calculated band gaps of CeO_2 and CeF_3 are 3.20 eV and 3.38 eV, respectively, which are consistent with the experimental value of 3.23 eV and 3.32 eV derived from the UV-visible spectra (Fig. 4). Fig. 8(b) shows that the upper part of valence band of CeO_2 is dominated by O 2p states, while the narrow band situated just above the Fermi level is mainly due to 4f states of Ce. Therefore, the pure CeO_2 shows an onset of optical absorption about 390 nm, which is attributed to the intrinsic transition from O 2p to Ce 4f states (3.2 eV), in agreement with the UV-Vis absorption spectrum (Fig. 4(a)). By contrast, both the upper part of valence band and the bottom of conduction band of CeF_3 are composed primarily of Ce 4f states, mixing with a small F 2p states (Fig. 8(a)). The shape of the absorption curve (Fig. 4(a)) of CeF_3 indicates that CeF_3 is an indirect semiconductor, which can be verified by the band structure (Figs.8(c), (d) and (e)). Therefore, the smooth upward absorption curve from 600 nm to 250 nm, as shown in Fig. 4(a), of CeF_3 cannot be ascribed to the transitions between valence band and conduction band. The optical absorption of CeF_3 in the visible light region is closely related to the defect levels appeared in the band gap. It is generally considered that the defects and the degree of disorder in the nanomaterials is relatively high, and thereby a lower crystal field symmetry might be induced and give rise to the change in the absorption spectra[27]. In this work, the CeF_3 nanoparticles prepared by low-temperature solution combustion are hard to avoid intrinsic defects, such as cerium and oxygen vacancies, especially at the surfaces of nanoparticles. It is reasonable to suppose that the optical absorption of CeF_3 in the visible light (Fig. 4(a)) can be attributed to the defects in the samples. In particular, the DOS, just below the Fermi level, of CeF_3 is much larger than that of CeO_2 (see Figs. 8 (a) and (b)). Thus, the values of f−f and p−f matrix elements of the imaginary part of the dielectric function due to direct interband transitions are large, which is one of the key factors for higher photocatalytic activity of CeF_3.

4. Conclusions

Novel photocatalyst CeF_3 is prepared by a facile low-temperature solution combustion method. Pure CeF_3 nanoparticles, its mixture with CeO_2 and/or Ce_2O_3, and pure CeO_2 nanoparticles can be obtained by adjusting the molar ratios of ammonium fluoride to cerium chloride. The synthesized CeF_3 samples are mesopore nanoparticles with specific surface area of 11.3 $m^2 g^{-1}$. It is interesting that the synthesized CeF_3 samples show excellent photocatalytic activity and good stability for MB degradation under UV light irradiation. Experiments combined with the DFT calculation reveal that the unique electronic structure of CeF_3 may be an important reason for the enhanced photocatalytic performance of CeF_3. The present work demonstrates the efficient photocatalytic activity of CeF_3, which can be applied as a potential photocatalyst.

Acknowledgments

This work is supported by the Changsha Science and Technology Plan Projects, China (Grant No. K1403067-11).

References

1. Z. G. Yi, J. H. Ye, N. Kikugawa, T. Kako, S. X. Ouyang, H. Stuart-Williams, H. Yang, J. Y. Cao, W. J. Luo, Z. S. Li, Y. Liu and R. L. Withers, *Nat Mater.*, 2010, 9, 559-564.
2. Z. M. Yang, G. F. Huang, W. Q. Huang, J. M. Wei, X. G. Yan, Y. Y. Liu, C. Jiao, Z. Wan and A. L. Pan, *J. Mater. Chem.A*, 2014, 2, 1750-1756.
3. J. Di, J. Xia, S. Yin, H. Xu, M. He, H. Li, L. Xu and Y. Jiang, *RSC Adv.*, 2013, 3, 19624-19631.
4. L. Xu, W. Q. Huang, L. L. Wang, Z. A. Tian, W. Y. Hu, Y. M. Ma, X. Wang, A. L. Pan and G. F. Huang, *Chem. Mater.*, 2015, 27, 1612-1621.
5. J. G. Yu, Y. R. Su and B. Cheng, *Adv. Funct. Mater.*, 2007, 17, 1984-1990.
6. B. C. Qiu, Y. Zhou, Y. F. Ma, X. L. Yang, W. Q. Sheng, M. Y. Xing and J. L. Zhang, *Sci. Rep-Uk*, 2015, 5.
7. X. B. Wang, Y. Yan, B. Hao and G. Chen, *Dalton Trans.*, 2014, 43, 14054-14060.
8. Z. L. Ma, G. F. Huang, D. S. Xu, M. G. Xia, W. Q. Huang and Y. Tian, *Mater. Lett.*, 2013, 108, 37-40.

9. W.-J. Ong, M. M. Gui, S.-P. Chai and A. R. Mohamed, *RSC Adv.*, 2013, 3, 4505-4509.

10. H. Wan, L. Xu, W. Q. Huang, J. H. Zhou, C. N. He, X. F. Li, G. F. Huang, P. Peng and Z. G. Zhou, *RSC Adv.*, 2015, 5, 7944-7952.

11. C. Yu, G. Li, S. Kumar, K. Yang and R. Jin, *Adv. Mater.*, 2014, 26, 892-898.

12. H. Xu, J. Yan, Y. Xu, Y. Song, H. Li, J. Xia, C. Huang and H. Wan, *Appl. Catal., B*, 2013, 129, 182-193.

13. Y. Peng, M. Yan, Q.-G. Chen, C.-M. Fan, H.-Y. Zhou and A.-W. Xu, *J. Mater. Chem.*, 2014, 2, 8517-8524.

14. I. Aslam, C. Cao, M. Tanveer, M. H. Farooq, W. S. Khan, M. Tahir, F. Idrees and S. Khalid, *RSC Adv.*, 2015, 5, 6019-6026.

15. R. Di Monte and J. Kaspar, *J. Mater. Chem.*, 2005, 15, 633-648.

16. L. Xu and J. Wang, *Environ. Sci. Technol.*, 2012, 46, 10145-10153.

17. Y.-Y. Chu, Z.-B. Wang, Z.-Z. Jiang, D.-M. Gu and G.-P. Yin, *Adv. Mater.*, 2011, 23, 3100-+.

18. W. D. Zhang, D. L. Tang, X. P. Zhou, H. L. Wan and K. R. Tsai, *J. Chem. Soc., Chem. Commun.*, 1994, 771-772.

19. A. L. Mosse, A. V. Gorbunov, A. G. Doroshkevitch and V. N. Ivanova, *High Temp. Mater. Processes (New York)*, 2011, 15, 253-258.

20. P. Ji, J. Zhang, F. Chen and M. Anpo, *J. Phys. Chem. C*, 2008, 112, 17809-17813.

21. F. Chen, Y. Cao and D. Jia, *Appl. Surf. Sci.*, 2011, 257, 9226-9231.

22. C. N. Tang, W. Q. Hou, E. Z. Liu, X. Y. Hu and J. Fan, *J. Lumin.*, 2014, 154, 305-309.

23. Y. Chen, T. M. Liu, C. L. Chen, W. W. Guo, R. Sun, S. H. Lv, M. Saito, X. H. Peng, S. Tsukimoto and Z. C. Wang, *Physica E*, 2013, 48, 181-186.

24. Y. Y. Li and S. Q. Xu, *J. Alloys Compd.*, 2014, 601, 195-200.

25. D. P. Feng, W. M. Liu and Q. J. Xue, *Mater. Sci. Eng.A*, 2002, 326, 195-201.

26. Máté Kovács, Zsolt Valicsek, Judit Tóth, László Hajba, éva Makó, Pál Halmos, *Colloid Surfaces A*, 2009, 352, 56–62

27. L.Zhu, Q.Li, X. D.Liu, J. Y.Li, Y. F.Zhang, J.Meng and X. Q.Cao, *J. Phys. Chem. C*, 2007, **111**, 5898-5903

28. Y. Liu, Yanbao Zhao, Laigui Yu, Zhishen Wu, Journal of Alloys and Compounds, 2009, 485, L1–L4

29. X.Y. Pan, M.Q. Yang,; X.Z.Fu, et al., *Nanoscale*, 2013. 5(9), 3601-3614.

30. M.M.Khan, S. A. Ansari, D.Pradhan, et al., *J. Mater. Chem.A*, 2014, 2(3), 637-644.

31. D. A.Kumar, S.Selvasekarapandian, H.Nithya, and Y. Masuda, Solid State Sci, 2012. **14**, 626-634

32. R.F Zuo, G. X.Du, W. W.Zhang, L. H. Liu, Y. M. Liu, L. F.Mei and Z. H.Li, Adv Mater Sci Eng, 2014. 170148-1-7

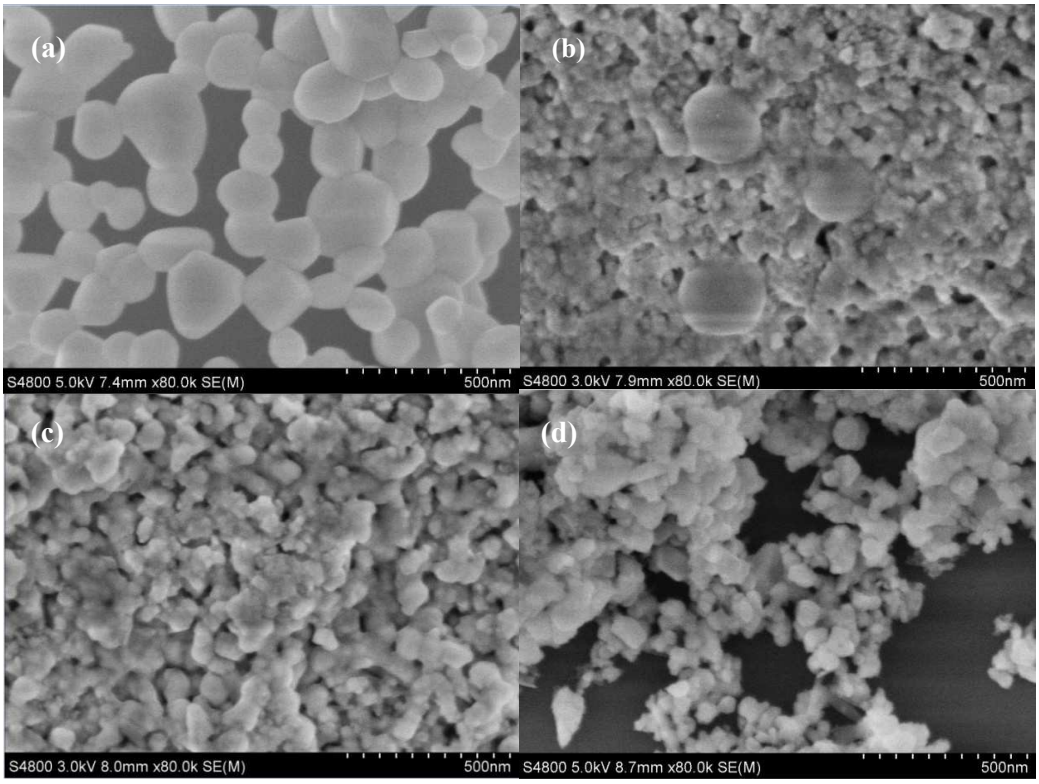

Fig.1. SEM images of prepared samples. (a) sample A, (b) sample B, (c) sample C and (d) sample D

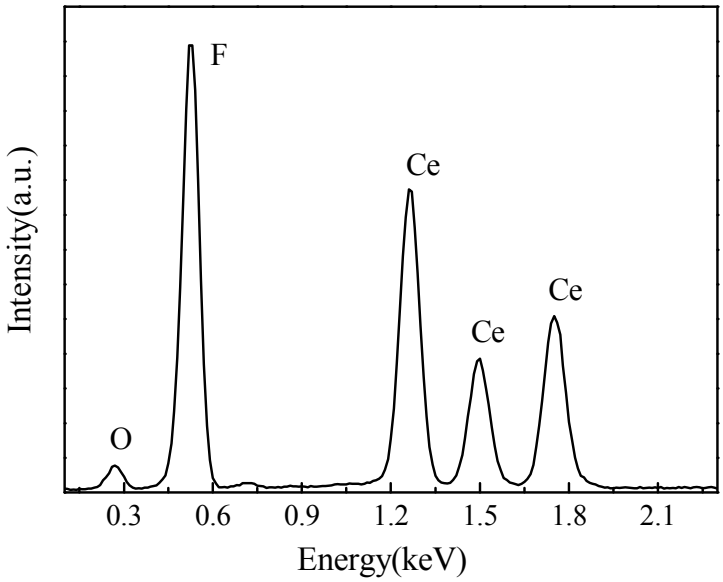

Fig.2. EDS spectrum of sample B

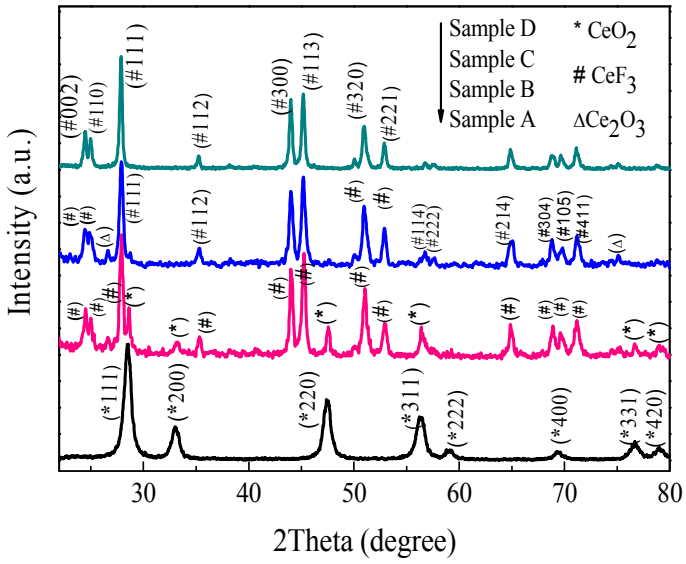

Fig.3. XRD patterns of as-prepared samples.

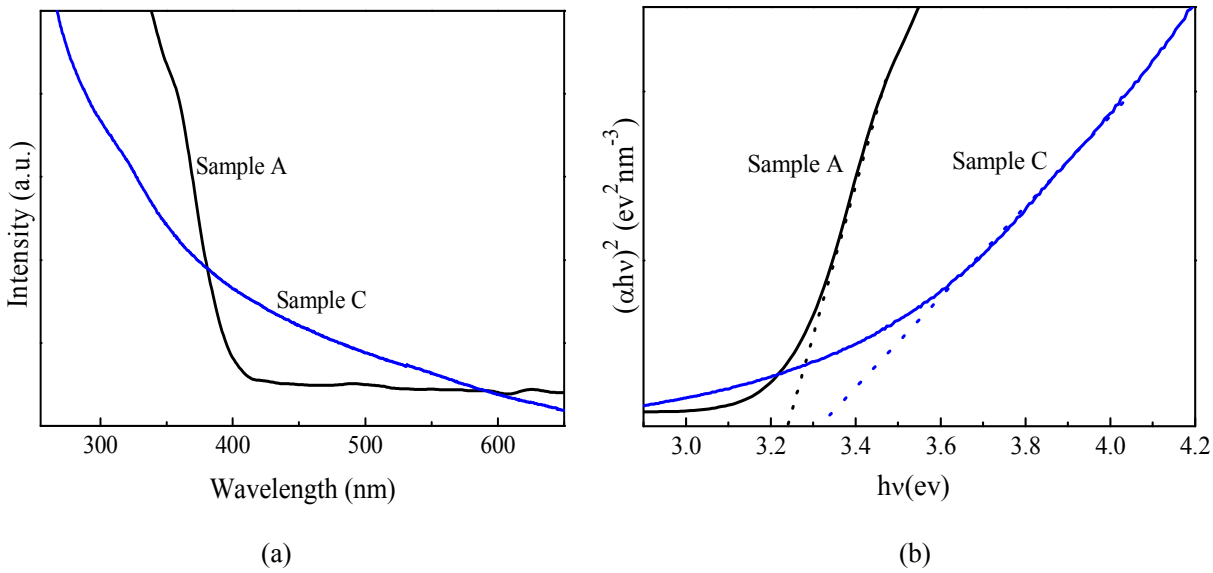

Fig.4. (a) UV-Vis absorption spectra of sample A and C, (b) Band gaps of sample A and C.

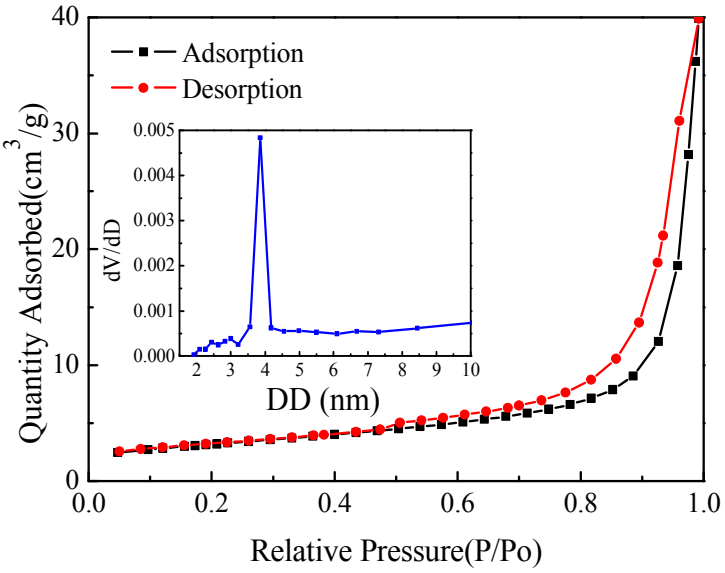

Fig. 5. Adsorption-desorption curve of sample C.

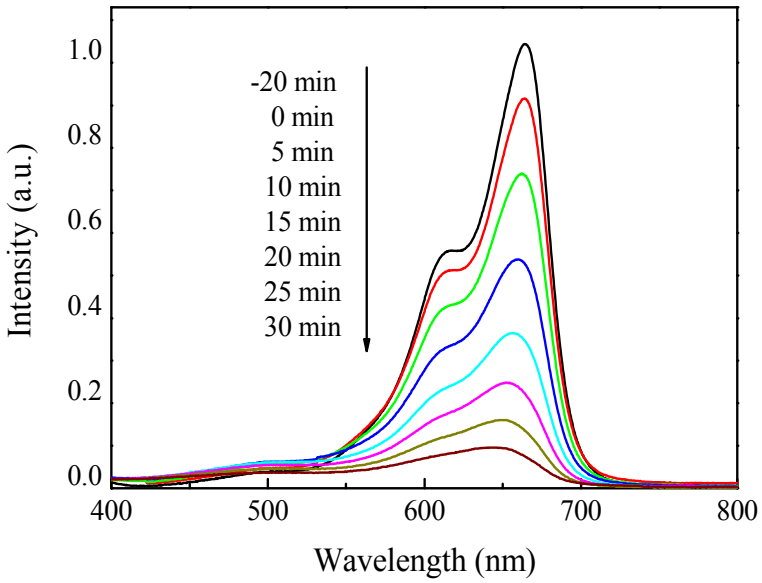

(a)

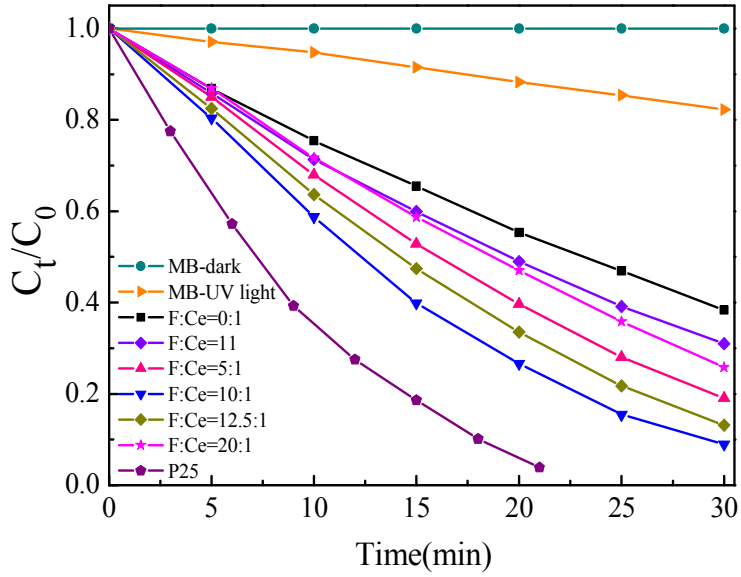

(b)

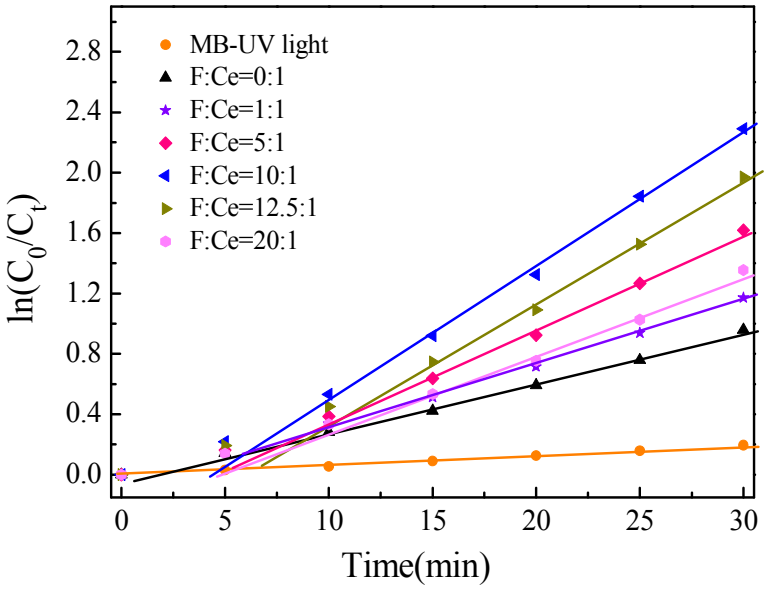

(c)

Fig.6. (a) Time dependence of the UV–vis spectra in photodegradation of MB of sample C, (b) The comparisons of photocatalytic activities of different samples for the photodegradation of MB under UV light irradiation, (c) The kinetic curves of samples.

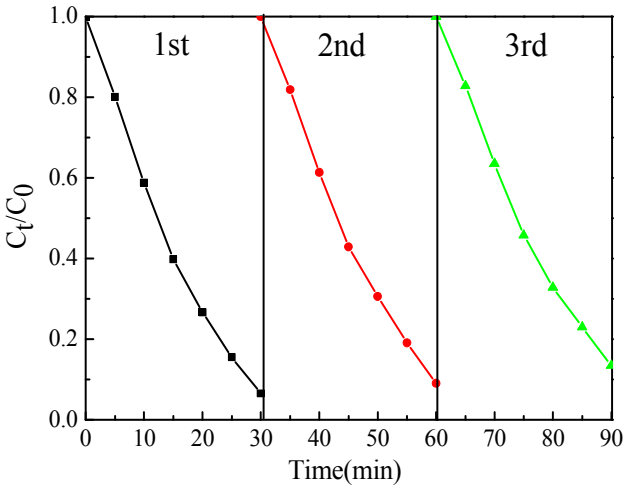

Fig.7. Cycling runs of sample C in the photodegradation of MB under UV light irradiation.

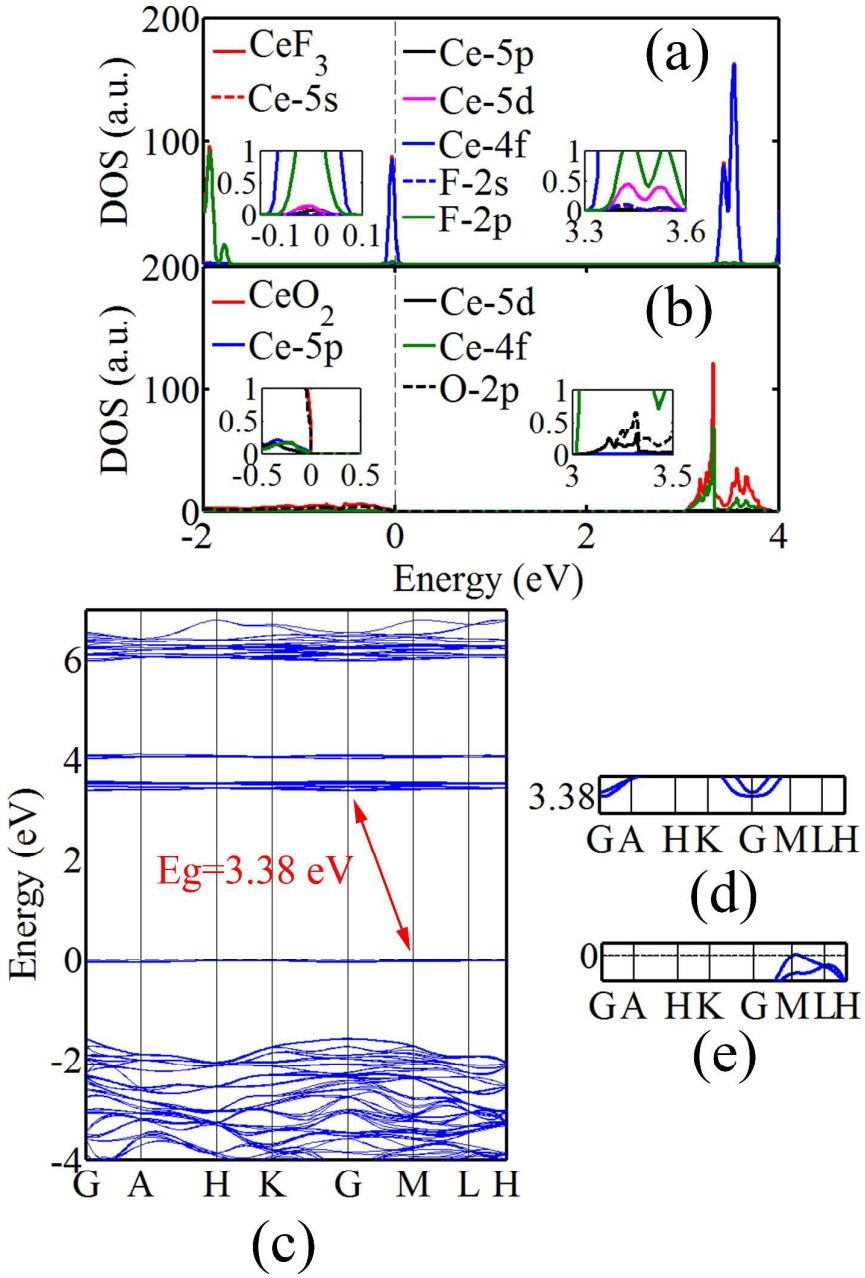

Fig. 8. Density of state (DOS) and the projected DOS (PDOS) of (a) CeF_3, (b) CeO_2. (c) Band structure of CeF_3. The zoom view of (d) the bottom of conduction band and (e) the top of valence band